

Biochemistry. Author manuscript, available in Fivic 2014 October 13

Published in final edited form as:

Biochemistry. 2013 October 15; 52(41): . doi:10.1021/bi400852h.

Elucidating features that drive the design of selective antifolates using crystal structures of human dihydrofolate reductase

Kristen M. Lamb, Narendran G-Dayanandan, Dennis L. Wright, and Amy C. Anderson* Department of Pharmaceutical Sciences, University of Connecticut, 69 N. Eagleville Rd., Storrs, CT 06269

Abstract

The pursuit of antimicrobial drugs that target dihydrofolate reductase (DHFR) exploits differences in sequence and dynamics between the pathogenic and human enzymes. Here, we present five crystal structures of human DHFR bound to a new class of antimicrobial agents, the propargyllinked antifolates (PLAs), with a range of potency (IC₅₀ values $0.045 \,\mu\text{M} - 1.07 \,\mu\text{M}$) for human DHFR. These structures reveal that interactions between the ligands and Asn 64, Phe 31 and Phe 34 are important for increased affinity to human DHFR and that loop residues 58-64 undergo ligand-induced conformational changes. The utility of these structural studies was demonstrated through the design of three new ligands that reduce contacts with Asn 64, Phe 31 and Phe 34. Synthesis and evaluation shows that one of the designed inhibitors exhibits the lowest affinity for human DHFR of any of the PLAs (2.64 µM). Comparisons of structures of human and Staphylococcus aureus DHFR bound to the same PLA reveal a conformational change in the ligand that enhances interactions with residues Phe 92 (Val 115 in huDHFR) and Ile 50 (Ile 60 in huDHFR) in S. aureus DHFR, yielding selectivity. Likewise, comparisons of human and Candida glabrata DHFR bound to the same ligand show that hydrophobic interactions with residues Ile 121 and Phe 66 (Val 115 and Asn 64 in human DHFR) yield selective inhibitors. The identification of residue substitutions that are important for selectivity and the observation of active site flexibility will help guide antimicrobial antifolate development for the inhibition of pathogenic species.

Dihydrofolate reductase (DHFR) is an essential metabolic enzyme that plays a critical role in one-carbon transfer reactions, including the biosynthetic pathways for deoxythymidine monophosphate (dTMP), purines and several amino acids. As such, DHFR has been successfully targeted for both anticancer (eg. methotrexate) and antimicrobial (eg. trimethoprim, pyrimethamine) drug development. Owing to its essential role in both human and pathogenic cells, the successful development of antimicrobial DHFR inhibitors requires that the compounds are selective for the pathogenic species.

While the function of DHFR is highly conserved throughout evolution, the amino acid sequence of the protein differs between species, allowing the design of inhibitors that are specific for pathogenic enzymes. High resolution structures of human DHFR that provide the spatial and dynamic information necessary for exploiting sequence differences are critical in the design of antimicrobial antifolates. For example, the design of selective antifolates effective against opportunistic infections *Pneumocystis jirovecii*(1-7) and *Toxoplasma gondii*(8) as well as the parasite that causes malaria, *Plasmodium*

^{*}Corresponding author: Amy C. Anderson, University of Connecticut, 69 N. Eagleville Rd, Storrs, CT 06269, ph: 860-486-6145, fax: 860-486-6857; amy.anderson@uconn.edu.

Supporting Information. Additional figures of ligands, structural alignment of human, *S. aureus* and *C. glabrata* DHFR and superpositions of human DHFR crystal structures. This material is available free of charge via the Internet at http://pubs.acs.org.

falciparum(9), were all enabled by structures of human DHFR. The available ternary structures of human DHFR are important guides toward the design of selective antifolates against these and other pathogenic species. However, additional structures of human DHFR bound to ligands with new scaffolds that explore conformational changes and probe sequence differences would support a more complete understanding of the factors that drive antifolate potency and selectivity.

We have been developing propargyl-linked antifolates (PLAs) to target several therapeutic indications including bacterial infections caused by methicillin-resistant *Staphylococcus aureus* (MRSA) and *Bacillus anthracis* as well as fungal infections caused by *Candida glabrata* and *Candida albicans*(10-18). Toward this goal, we have used structure-activity relationships and modeling studies with human DHFR to design compounds selective for the pathogenic enzyme. For example, a PLA with a substituted biphenyl moiety shows 2350-fold greater potency for DHFR from *C. glabrata* (inhibition concentration 50 % (IC $_{50}$ = 0.6 nM) over human DHFR (IC $_{50}$ = 1.4 μ M) (16). Recently, we probed the role of critical loop residues at the active site (residues 58-64 in human DHFR) believed to influence selectivity using crystal structures of *C. glabrata* and *C. albicans* DHFR combined with molecular dynamics simulations of these enzymes and human DHFR. These studies show that the loop residues are flexible and assume a ligand-dependent conformation that is independent of species (19).

Here, we present five crystal structures of human DHFR bound to PLAs with a greater than 20-fold range of potency. As these ligands differ by positional substitutions and also represent a new chemotype bound to human DHFR, they are important for probing key interactions that drive potent interactions with human DHFR. Specifically, a comparison of these crystal structures with each other shows that hydrophobic interactions with Phe 31 and Phe 34 and hydrogen bonding with Asn 64 are important for increased potency for human DHFR. Based on these observations, we synthesized three compounds designed to reduce these contacts. Excitingly, compound UCP1075 loses 16-fold affinity for human DHFR while maintaining potent antibacterial activity. As we have previously determined crystal structures of C. glabrata(19) and S. aureus DHFR (20) bound to one of these compounds, a comparison across three species bound to the same ligand reveals the influence of the propargylic substitution and the hydrophobicity of the pyridyl ring toward selectivity. Comparisons of these structures with previously reported structures of human DHFR reinforce that the loop residues (58-64) undergo ligand-induced conformational changes. The structures and analysis reported here will not only aid the discovery of increasingly selective PLAs, but will be valuable for understanding the dynamics of the active site of human DHFR and elucidating the factors that drive potency and selectivity for a broad range of ligands.

Materials and Methods

Cloning, expression, and purification

The gene for human DHFR (huDHFR) was amplified from human genomic DNA, cloned into the pET-41a (+) vector (EMD Millipore) and used to transform competent BL21(DE3) *E. coli* cells. Expression of the protein was induced using IPTG at 30°C for 6 hours and terminated by harvesting cells via centrifugation. Cells were lysed with B-Per Protein Extraction Reagent (Thermo Scientific), DNase I (New England Biosciences), and 1 mM phenylmethylsulfonyl fluoride (PMSF; Sigma -Aldrich) at room temperature for 30 minutes. Soluble lysate, isolated by centrifuging the crude lysate, was exposed to 60% saturated ammonium sulfate overnight at 4°C. Contaminant proteins were removed from the crude protein sample by centrifugation. The prepared supernatant was applied to a methotrexate-agarose column (Sigma-Aldrich), washed and eluted with dihydrofolate (Sigma-Aldrich).

Fractions containing huDHFR were collected, concentrated and separated using an S-200 column. Resulting pure huDHFR was concentrated to 8 mg/mL, flash frozen and stored at -80°C until needed.

The synthesis and characterization of compounds UCP1006, UCP1015, UCP1017, UCP1019, UCP1025 and UCP1040 has been previously reported (19-21). Compounds UCP1075-1077 were synthesized with routes analogous to those previously published (19-21).

Enzyme Inhibition Assays

Enzyme inhibition assays were performed by measuring the rate of NADPH oxidation by the enzyme at 340 nm over time. Assays were completed at room temperature in buffer containing 20 mM TES, 50 mM potassium chloride, 0.5 mM EDTA, 10 mM ß-mercaptoethanol, and 1 mg/mL bovine serum albumin. Limiting concentrations of enzyme and an excess of NADPH (100 μ M) were added to the buffer, followed by DHF (100 μ M), initiating DHFR activity. The ligand was incubated with the protein and NADPH prior to the addition of DHF. Values for racemic mixtures of UCP1006, UCP1019, UCP1040, UCP1075-1077 were measured. All measurements were repeated at least three times; averaged IC50 values and standard deviations are reported.

Crystallization

Pure human DHFR (8 mg/mL) was incubated for 2.5 hours on ice with 1 mM NADPH and 1 mM ligand (racemic mixtures for UCP1006 and UCP1019). The protein sample was concentrated to 11-15 mg/mL and added in a 1:1 ratio to the crystallization tray reservoir solution. The reservoir solutions contained 0.1 M Tris pH 7.5, 0.2 M or 0.3 M lithium sulfate, 23-33% (w/v) PEG 4000, and 6-8% (v/v) ethanol or 1% (v/v) trifluoroethanol. Nonvolatile additives were also used in most cases, except in the case of the ternary structure with UCP1017. These included strontium (II) chloride, calcium chloride, and magnesium chloride, which were added to the 1:1 ratio protein sample: reservoir solution for final concentrations of 11 mM. Crystals were grown using the hanging-drop vapor diffusion method at 4 °C. Crystals were flash frozen with liquid nitrogen using 15% (v/v) ethylene glycol as a cryo-protectant. Diffraction data for the huDHFR/NADPH/ UCP1006 crystal were obtained at the University of Connecticut X-Ray Crystallography Facility with an R-Axis IV++, and processed using Rigaku Structure Studio Process. Data for the remaining four crystals were obtained at Brookhaven National Laboratory using beamline X4A. Data were processed with HKL2000.

Structure determination

Initial evaluation of data quality and estimated Matthew's coefficient were determined using Matthews_coef, CCP4i 6.20 package and/or Xtriage in Phenix-1.8-1069 (22). All structures were determined with molecular replacement using Phaser, part of the CCP4i 6.20 package (23), with human DHFR structures, PDB ID 2C2S(24) or 2W3A(25), in the case of huDHFR/NADPH/ UCP1015. Prodrg was used to produce cif and pdb files of the ligands (26). The model was built using Refmac (27) and Coot (28). Refinement continued in Phenix-1.8-1069 (22). The electron density for the complexes of huDHFR/NADPH/ UCP1017 and huDHFR/NADPH/ UCP1019 showed one molecule of huDHFR bound to NADPH and the propargyl-linked ligand and one molecule of huDHFR bound to NADPH and dihydrofolate per asymmetric unit.

Results

Propargyl-linked Antifolates

In pursuit of high resolution crystal structures to guide designs for more selective antifolates, we crystallized human DHFR with five PLAs (UCP1006, UCP1015, UCP1017, UCP1019 and UCP1025; Table 1). The antifolates include a 2,4-diamino-6-ethyl-pyrimidine ring (ring A) and a biaryl ring system (rings B and C) united by a propargyl linker. The antifolates for this study were specifically chosen as they have varying affinities for human DHFR (19, 20) and could be used to probe the basis of potency for human DHFR. For example, 50% inhibition concentration (IC $_{50}$) values for these ligands in enzyme inhibition assays range from 0.045 μM to 1.07 μM (Table 1). The ligands differ in the substitution pattern at the propargylic linker (hydrogen or methyl) and the biaryl ring system (3,5 pyrimidine, 4-pyridine or isoquinoline). Crystal structures of human DHFR with these related pairs of ligands probe the roles of specific residues in determining potency; comparisons with structures from pathogenic enzymes reveal the features that determine selectivity.

Ternary Structures of Human DHFR

Diffraction data were collected from flash-frozen crystals of ternary complexes of human DHFR (huDHFR) bound to the cofactor, NADPH and ligand. All five ternary crystals belong to space group C222₁ and contain two protein molecules within the asymmetric unit. Structures with UCP1006, UCP1025, UCP1017 and UCP1019 were determined using molecular replacement with the structure of human DHFR from PDB ID: 2C2S (24) as a probe molecule; the structure with UCP1015 was determined with probe PDB ID: 2W3A (25). Data collection and refinement statistics are summarized in Table 2 and representative electron density is shown in Supporting Information Figure S1. The models superimpose with minimal root mean square deviations (RMSD). Using huDHFR/NADPH/ UCP1006 as a reference, the RMSD measurements with models bound to ligands UCP1015, UCP1017, UCP1019, and UCP1025 are 0.234, 0.146, 0.116, and 0.132 Å respectively.

The interactions of the 2,4-diaminopyrimidine ring are conserved throughout the structures and anchor the ligand in the active site (Figure 1). The 4-amino moiety forms a hydrogen bond with the backbone carbonyl oxygen of Ile 7 along with a weak hydrogen bond with the backbone carbonyl oxygen of Val 115 (3.47 Å). Atom N1 and the 2-amino group form hydrogen bonds with Glu 30. Additionally, residues Phe 34 and Ile 7 form hydrophobic interactions with the pyrimidine ring.

Here, we compare two structures of human DHFR bound to ligands with methyl substituents at the propargylic position (UCP1006 and UCP1019) and three bound to ligands with hydrogen at this position (UCP1025, UCP1017, UCP1015). The structures of huDHFR bound to UCP1006 (Fig. 1a) and UCP1019 (Fig. 1c) show that the ligands adopt similar conformations and the same configuration at the stereogenic center. Specifically, the dihedral angle defined by C5 of the diaminopyrimidine, the propargylic carbon and the C1' and C2' of the B-ring varies by only 10.68° between UCP1006 (-96.55) and UCP1019 (-107.23). However, hydrogen at the propargylic position affords the ligand greater flexibility. The same dihedral angle defined as above is -106.5°, -118.2° and 80.4° for UCP1015 (Fig. 1b), UCP1017 (Fig. 1d) and UCP1025 (Fig. 1e), respectively (a superposition of ligands showing the variation between dihedral angles is shown in Supporting Information Figure S2). Altering the dihedral angle allows the ligands to maximize interactions, contributing to the observed changes in potency. For example, a comparison of structures bound to UCP1006 ($IC_{50} = 1.3 \mu M$) or UCP1015 ($IC_{50} = 61 n M$; Fig. 2a), shows that the pyridyl ring of UCP1015 forms increased van der Waals interactions with Leu 67 (3.5 Å as opposed to 3.7 Å) and Phe 34 (3.7 Å compared to 4.64 Å).

Compound UCP1017, with hydrogen at the propargylic position, differs from compound UCP1019 only in the substitution of a methyl at this position. While the dihedral angle across the propargyl linker, as defined above, varies by only 11 $^{\circ}$ between the two ligands, the flexibility of UCP1017 aids in the formation of hydrophobic interactions with Phe 31 and Phe 34 (Fig. 2b), both of which are weaker with UCP1019. Both UCP1017 and UCP1019 are unique among the ligands presented here in that they form hydrogen bonds with Asn 64: UCP1017 forms one hydrogen bond (3.2 Å) and UCP1019 forms two hydrogen bonds (2.9 and 3.1 Å). This increased number of hydrogen bonds in the structure with UCP1019 overcomes the weaker hydrophobic interactions with Phe 31 and Phe 34, resulting in comparable IC50 values (UCP1019: 0.045 μM and UCP1017: 0.060 μM).

Compound UCP1025 varies from UCP1015 in that it possesses a pyrimidyl C-ring as opposed to a pyridyl C-ring and a phenyl as opposed to a methoxy-phenyl in the B ring. As noted previously, the dihedral angle of UCP1025 is 80.41° , which is the opposite sign from the other ligands (Figs. 2c and S2). This alternate angle forces the B-ring of UCP1025 "backward" toward Phe 34 and Leu 67 relative to its position in the other ligands where it is positioned to interact strongly with Ile 60. The alternate orientation of UCP1025 appears to be driven by a combination of the hydrophobic interactions with Pro 61 and the presumed interaction between the basic nitrogen and bulk solvent. The minimal interactions observed for compound UCP1025, including weak hydrophobic interactions with Leu 67 (3.50 Å) and Pro 61 (3.86 Å), rationalize its lower IC50 value (0.33 μ M) compared to UCP1015 (0.061 μ M).

Design, Synthesis and Evaluation of New Ligands

As interactions between the inhibitor and residues Phe 31, Phe 34 and Asn 64 appear to drive potency for human DHFR, three new ligands were designed to limit contacts with these residues. The scaffold for these new ligands was derived from lead compound UCP1040 (Table 1) that exhibits superior metabolic stability relative to UCP1006 (21). UCP1040, with a propargylic methyl and 2'-methoxy substitutions, inhibits human DHFR with an IC₅₀ value of 0.164 μM. Inhibitor UCP1075 places a methyl group ortho to the biaryl linkage, thus destabilizing the coplanar conformation observed in many of these inhibitors. The more perpendicular arrangement of these two rings is intended to effectively force the C-ring into the crowded space between Phe 31 and Pro 64 and create negative steric interactions with Phe 31 (see Figure 1a for reference). As an alternative design, compounds UCP1076-1077, with 3,5-dimethyl or 3-methoxy substituents, respectively, were intended to probe the effect of placing hydrophobic substitutions on the meta positions of the C-ring to reduce any favorable contacts with Asn 64. All three compounds were synthesized through previously published routes (19-21) using commercially available boronic acids. Excitingly, the simple methyl substitution on UCP1075 lowers affinity for human DHFR to 2.64 µM, a reduction of 16-fold relative to the parent UCP1040. Ligands UCP1076 and UCP1077 also reduce binding to human DHFR by approximately 2-fold. Importantly, all three compounds maintain antibacterial activity against the pathogenic organism MRSA at levels similar to that of other potent compounds in this series (MIC values $< 0.5 \,\mu g/mL)$ (20).

Docking UCP1075 to the structure of human DHFR confirmed the hypothesis that the methyl group forces a perpendicular arrangement of the ring system that creates significant steric interference with the active site residues. Two clusters of poses were obtained, both of which show atoms from the C-ring within only 3 Å of Leu 67 and Phe 31/34 (Figure 3).

Comparison of structures of human and pathogenic species of DHFR

Previously, we reported crystal structures of DHFR from *Candida glabrata*(19) and *S. aureus*(20) bound to NADPH and UCP1006. As we now describe a structure of human DHFR bound to these same ligands, we are in a position to capitalize on a direct comparison between the human and pathogenic enzymes in order to elucidate factors that drive selectivity without confounding differences in ligand-induced conformational changes.

The structures of huDHFR/NADPH/UCP1006 and CgDHFR/NADPH/UCP1006 show minimal overall differences (RMSD value of 1.14 Å) and the selection of the same enantiomer of the ligand (Fig. 2d). The marked difference in potency for UCP1006 between human DHFR (IC₅₀=1.07 μM) and C. glabrata DHFR (IC₅₀=89 nM) relates to interactions with species- specific residues (see Supporting Information Figure S2 for sequence alignment). A primary site of differential interactions lies in the contacts of the propargylic methyl group with residues in the active sites. In the structure of C. glabrata DHFR bound to UCP1006, the methyl group forms a hydrophobic interaction with Ile 121 (3.67 Å) while in human DHFR, there is little or no interaction with the corresponding Val 115 (4.37 Å). A second noteworthy difference between these species centers on the formation of hydrophobic interactions between Phe 66 of C. glabrata DHFR and the pyridine ring. In contrast, the pyridine ring is unable to form either hydrophobic interactions with the alkyl portion of the corresponding residue, Asn 64 in human DHFR, or a hydrogen bond with Asn 64. In human DHFR, the pyridine ring forms hydrophobic interactions with Phe 31, while the corresponding residue, Met 33 in C. glabrata DHFR, is further (0.5 Å) and forms only weak interactions. The hydrophobic interactions with Phe 31 in human DHFR do not overcome the loss of interactions at the Asn 64 and Val 115 positions, rationalizing the lower potency of this compound for human DHFR.

Superimposing the ternary structures of *S. aureus* and human DHFR bound to NADPH and UCP1006 reveals differences (Fig. 2e), some of which explain the selectivity of UCP1006 toward *S. aureus* DHFR (Sa: IC₅₀=19 nM). Overall, the two structures have an RMSD of 1.15 Å. The first notable difference is that the diaminopyrimidine ring of *S. aureus* DHFR maintains the conserved interactions but shifts 0.7-0.8 Å toward Phe 92 in order to enhance van der Waals interactions with the phenyl side chain. Secondly, the torsional angle previously defined across the propargyl linker is 126.79° in UCP1006 when bound to *S. aureus* DHFR and -96.55° when bound to human DHFR. The angle adopted by UCP1006 when bound to *S. aureus* DHFR allows the ligand to optimize hydrophobic interactions with Phe 92, Ile 50 and Leu 54. While Ile 50 and Leu 54 are conserved in human DHFR, the hydrophobic interactions between the ligand and these residues are much stronger in *S. aureus* DHFR. The interactions between the propargyl linker and Phe 92, which is Val 115 in human DHFR, are unique to *S. aureus* DHFR. It is these increased hydrophobic interactions with Phe 92, Ile 50 and Leu 54 that explain the greater potency of UCP1006 for *S. aureus* DHFR over human DHFR.

Conformational Changes and Interpretation of Dynamics

Previously, we reported that molecular dynamics simulations of human DHFR revealed that the loop residues 58-64 undergo ligand-induced conformational changes (19). While the overall RMSDs between these structures of human DHFR are minimal, there are several indications that the protein is flexible. For example, the structures with UCP1006 and UCP1017 show two different rotamers for Phe 31 with 62 % and 38 % occupancy. Interestingly, the structure of human DHFR bound to piritrexim (PDB ID: 1DLR(29)) selects one of these rotamers while the structure with SRI-9662 (PDB ID: 1KMV(8)) selects the other. A superposition of the structures bound to the PLAs show that the loop residues (58-64) undergo ligand-induced conformational changes, confirming the results obtained

previously by simulation. $C\alpha$ atoms of the residues in the loop are shifted 0.7 Å between the complexes with UCP1006 and UCP1025, with the residues in the latter complex forming tighter interactions with the ligand. Flexibility has been more widely observed for these loop residues; a superposition of eight structures of human DHFR bound to a variety of ligands shows notable variation (Fig. 4; distances between $C\alpha$ atoms reported in Supporting Information). Strikingly, superposition of the structure of huDHFR/NADPH/UCP1006 with huDHFR/NADPH/SRI-9662 (PDB ID:1KMV) shows that the loop residues are displaced by up to 2 Å between the two structures (Fig. 2f and Fig. 4). These interpretations of active site dynamics are important for amassing a complete picture of the factors that drive selectivity against the human enzyme.

Discussion

The development of antimicrobial antifolates demands that the compounds are optimally selective for the pathogenic species. We and others have actively pursued the development of antimicrobial DHFR inhibitors and have worked to fully elucidate the factors that drive selectivity against the human DHFR enzyme. Specifically, over the past several years we have been developing the PLAs as efficacious antibacterial and antifungal agents. Herein, we describe work to elucidate the critical interactions that drive potency and selectivity against human DHFR using five crystal structures of this enzyme bound to NADPH and the PLAs. The five ligands in these experiments possess different substitutions that can be used to probe the roles of active site residues in DHFR.

Previously reported efforts to develop selective antimicrobial antifolates targeting other pathogens have also described structures of human DHFR bound to antifolates of interest. For example, efforts to develop a novel antimalarial antifolate, P218 (9), compared structures of P218 with *Plasmodium falciparum* and human DHFR to reveal that the inhibitor adopts a very different conformation in human DHFR. In *P. falciparum* DHFR-TS, the inhibitor interacts with Phe 116 (equivalent to Phe 66 of CgDHFR) to drive the new conformation and form hydrogen bonds with Arg 122 (Pf). In human DHFR, the inhibitor forms interactions with Phe 31 that directs it away from potential hydrogen bonds with Arg 70 (equivalent to Arg 122 of PfDHFR). Development of a selective antifungal antifolate to target *Pneumocystis jirovecii* (PY957) relied on structures of *P. carinii* and human DHFR coupled with site-specific mutagenesis to reveal the basis of selectivity (5, 7). In this case, it was observed that interactions with the pathogen-specific residues at Gln 35 (Lys in *P. carinii* DHFR) and Asn 64 (Phe in *P. carinii* DHFR) were critical for selectivity.

Analysis of the crystal structures reported here reveals features of the PLAs that are critical for affinity to human DHFR; avoidance of these interactions should guide selectivity for the pathogenic species. Specifically, ligands should be designed to avoid groups that may form hydrogen bonds with Asn 64 as the structures reported here with compounds possessing isoquinoline C-rings show the affinity gained by these bonds. Furthermore, strong hydrophobic interactions with Phe 31 and Phe 34 are instrumental in driving increased affinity to human DHFR and should be avoided. In this work, these observations were validated by the design and synthesis of three new ligands, one of which shows a 16-fold reduction in affinity for human DHFR.

These studies add important evidence to drive the design of compounds with enhanced selectivity against *S. aureus* and *C. glabrata* DHFR. For example, the propargylic methyl substitution in *C. glabrata* DHFR forms a hydrophobic interaction with Ile 121 that it is unable to form with the human Val 115 residue. Additionally, a hydrophobic ring system at the C-ring position is critical for *C. glabrata* inhibition, as it interacts with Phe 66, but does not interact with the polar residue Asn 64 in human DHFR. Finally, ligands that form

hydrophobic interactions with residues Phe 92 and Ile 60 maximize selectivity for *S. aureus* DHFR. While the interactions with the pathogen-specific residue corresponding to Asn 64 have been known to be important for selectivity, the value of interactions with pathogen-specific residues at Val 115 is emphasized here.

Supplementary Material

Refer to Web version on PubMed Central for supplementary material.

Acknowledgments

We thank Dr. Kathleen Frey for the expression plasmid with human DHFR and Stephanie Reeve for testing the antibacterial activity of UCP1075-1077.

Funding: NIH (GM067542, AI073375, AI065143)

References

- 1. Cody V, Galitsky N, Luft J, Pangborn W, Queener S, Gangjee A. Analysis of quinazoline and pyrido[2,3-d]-pyrimidine N9-C10 reversed bridge antifolate in complex with NADP+ and *Pneumocystis carinii* dihydrofolate reductase. Acta Cryst. 2002; D58:1393–1399.
- Cody V, Galitsky N, Luft J, Pangborn W, Rosowsky A, Queener S. Structure-based enzyme inhibitor design: modeling studies and crystal structure analysis of *Pneumocystis carinii* dihydrofolate reductase ternary complex with PT653 and NADPH. Acta Cryst. 2002; D58:946–954.
- Cody V, Galitsky N, Rak D, Luft J, Pangborn W, Queener S. Ligand-Induced Conformational Changes in the Crystal Structures of *Pneumocystis carinii* Dihydrofolate Reductase Complexes with Folate and Nadp+ Biochemistry. 1999; 38:4303–4312. [PubMed: 10194348]
- Cody V, Luft J, Pangborn W, Gangjee A, Queener S. Structure determination of tetrahydroquinazoline antifolates in complex with human and *Pneumocystis carinii* dihydrofolate reductase: correlations between enzyme selectivity and stereochemistry. Acta Cryst. 2004; D60:646–655.
- Cody V, Pace J. Structural analysis of *Pneumocystis carinii* and human DHFR complexes with NADPH and a series of five potent 6-[5'-(w-carboxyalkoxy)benzyl]-pyrido[2,3-d]pyrimidine derivatives. Acta Cryst. 2011; D67:1–7.
- Cody V, Pace J, Chisum K, Rosowsky A. New insights into DHFR interactions: analysis of *Pneumocystis carinii* and mouse DHFR complexes with NADPH and two highly potent trimethoprim derivatives. Proteins. 2006; 65:959–969. [PubMed: 17019704]
- 7. Cody V, Pace J, Makin J, Piraino J, Queener S, Rosowsky A. Correlations of Inhibitor kinetics for *Pneumocystis jirovecii* and human dihydrofolate reductase with structural data for human active site mutant enzyme complexes. Biochemistry. 2009; 48:1702–1711. [PubMed: 19196009]
- Klon A, Heroux A, Ross L, Pathak V, Johnson C, Piper J, Borhani D. Atomic structures of human dihydrofolate reductase complexed with NADPH and two lipophilic antifolates at 1.09 A and 1.05 A resolution. J Mol Biol. 2002; 320:677–693. [PubMed: 12096917]
- Yuthavong Y, Tarnchompoo B, Vilaivan T, Chitnumsub P, Kamchonwongpaisan S, Charman S, McLennan D, White K, Vivas L, Bongard E, Thongpanchang C, Taweechai S, Vanichtanankul J, Rattanajak R, Arwon U, Fantauzzi P, Yuvaniyama J, Charman W, Matthews D. Malarial dihydrofolate reductase as a paradigm for drug development against a resistance-compromised target. Proc Natl Acad Sci. 2012; 109:16823–16828. [PubMed: 23035243]
- Beierlein J, Frey K, Bolstad D, Pelphrey P, Joska T, Smith A, Priestley N, Wright D, Anderson A. Synthetic and crystallographic studies of a new inhibitor series targeting *Bacillus anthracis* dihydrofolate reductase. J Med Chem. 2008; 51:7532–7540. [PubMed: 19007108]
- Bolstad D, Bolstad E, Frey K, Wright D, Anderson A. A structure-based approach to the development of potent and selective inhibitors of dihydrofolate reductase from *Cryptosporidium*. J Med Chem. 2008; 51:6839–6852. [PubMed: 18834108]

 Frey K, Liu J, Lombardo M, Bolstad D, Wright D, Anderson A. Crystal Structures of Wild-type and Mutant Methicillin-resistant *Staphylococcus aureus* Dihydrofolate Reductase Reveal an Alternative Conformation of NADPH that may be Linked to Trimethoprim Resistance. J Mol Biol. 2009; 387:1298–1308. [PubMed: 19249312]

- 13. Frey K, Lombardo M, Wright D, Anderson A. Towards the Understanding of Resistance Mechanisms in Clinically Isolated Trimethoprim-resistant, Methicillin-resistant *Staphylococcus aureus* Dihydrofolate Reductase. J Struc Biol. 2010; 170:93–97.
- 14. Frey K, Viswanathan K, Wright D, Anderson A. Prospectively screening novel antibacterial inhibitors of dihydrofolate reductase for mutational resistance. Antimicrob Agents and Chemother. 2012; 56:3556–3562. [PubMed: 22491688]
- 15. Liu J, Bolstad D, Bolstad E, Wright D, Anderson A. Towards New Antifolates Targeting Eukaryotic Opportunistic Infections. Euk Cell. 2009; 8:483–486.
- Liu J, Bolstad D, Smith A, Priestley N, Wright D, Anderson A. Structure-guided development of efficacious antifungal agents targeting *Candida glabrata* dihydrofolate reductase. Chem Biol. 2008; 15:990–996. [PubMed: 18804036]
- 17. Liu J, Bolstad D, Smith A, Priestley N, Wright D, Anderson A. Probing the active site of *Candida glabrata* dihydrofolate reductase with high resolution crystal structures and the synthesis of new inhibitors. Chem Biol Drug Des. 2009; 73:62–74. [PubMed: 19152636]
- 18. Paulsen J, Bendel S, Anderson A. Crystal structures of *Candida albicans* dihydrofolate reductase bound to propargyl-linked antifolates reveal the flexibility of active site residues critical for ligand potency and selectivity. Chem Biol Drug Des. 2011; 78:505–512. [PubMed: 21726415]
- Paulsen J, Viswanathan K, Wright D, Anderson A. Structural analysis of the active sites of dihydrofolate reductase from two species of Candida uncovers ligand-induced conformational changes shared among species. Bioorg Med Chem Lett. 2013; 23:1279–1284. [PubMed: 23375226]
- Viswanathan K, Frey K, Scocchera E, Martin B, Swain P, Alverson J, Priestley N, Anderson A, Wright D. Toward new Therapeutics for Skin and Soft Tissue Infections: Propargyl-linked Antifolates Are Potent Inhibitors of MRSA and *Streptococcus pyogenes*. PLoS ONE. 2012; 7:e29434. [PubMed: 22347365]
- 21. Zhou W, Viswanathan K, Hill D, Anderson A, Wright D. Acetylenic linkers in lead compounds: A study of the stability of the propargyl-linked antifolates. Drug Metab Distrib. 2012; 40:2002–2008.
- 22. Adams P, Afonine P, Bunkóczi G, Chen V, Davis I, Echools N, Headd J, Hung LW, Kapral G, Grosse-Kunstleve R, McCoy A, Moriarty N, Oeffner R, Read R, Richardson D, Richardson J, Terwilliger T, Zwart P. PHENIX: a comprehensive Python-based system for macromolecular structure solution. Acta Cryst. 2010; D66:213–221.
- 23. Potterton E, Briggs P, Turkenburg M, Dodson E. A graphical user interface to the CCP4 program suite. Acta Cryst. 2003; D59:1131–1137.
- 24. Reynolds R, Campbell S, Fairchild R, Kisliuk R, Micca P, Queener S, Riordan J, Sedwick WD, Waud W, Leung A, Dixon R, Suling W, Borhani D. Novel boron-containing, nonclassical antifolates: synthesis and preliminary biological and structural evaluation. J Med Chem. 2007; 50:3283–3289. [PubMed: 17569517]
- 25. Leung, A., Ross, L., Zywno-Van Ginkel, S., Reynolds, R., Seitz, L., Pathak, V., Barrow, W., White, E., Suling, W., Piper, J., and Borhani, D. (to be published).
- Schüttelkopf A, van Aalten D. PRODRG a tool for high-throughput crystallography of proteinligand complexes. Acta Cryst. 2004; D60:1355–1363.
- 27. Murshudov G, Vagin A, Dodson E. Refinement of macromolecular structures by the maximum-likelihood method. Acta Cryst. 1997; D53:240–255.
- Emsley P, Cowtan K. Coot: Model-building tools for molecular graphics. Acta Cryst. 2004; D60:2126–2132.
- 29. Lewis W, Cody V, Galitsky N, Luft J, Pangborn W, Chunduru S, Spencer HT, Appleman J, Blakley R. Methotrexate-resistant variants of human dihydrofolate reductase with substitutions of leucine 22. J Biol Chem. 1995; 270:5057–5064. [PubMed: 7890613]

Abbreviations

DHFR dihydrofolate reductase

huDHFR human dihydrofolate reductase
 IC₅₀ 50 % inhibition concentration
 dTMP deoxythymidine monophosphate

NADPH nicotinamide adenine dinucleotide phosphate

RMSD root mean square deviation



Figure 1.Propargyl-linked antifolates bound to human DHFR a) the active site of huDHFR/NADPH/ 1006; b) the active site of huDHFR/NADPH/1015; c) the active site of huDHFR/NADPH/ 1019; d) the active site of huDHFR/NADPH/1017; e) the active site of huDHFR/NADPH/ 1025

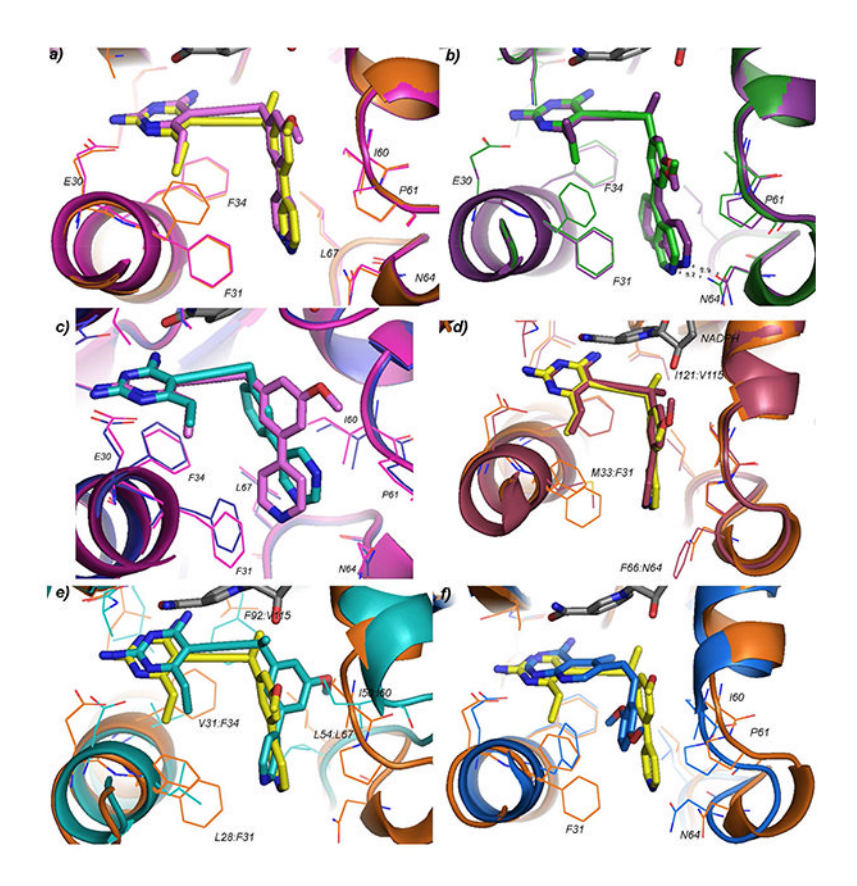


Figure 2. Superpositions of structures reveal features driving selectivity and conformational changes a) huDHFR/NADPH/1006 (orange, yellow) and huDHFR/NADPH/1015 (pink), b) huDHFR/NADPH/1017 (green) and huDHFR/NADPH/1019 (purple), c) huDHFR/NADPH/1015 (pink) and huDHFR/NADPH/1025 (cyan, purple) d) huDHFR/NADPH/1006 (orange, yellow) and CgDHFR/NADPH/1006 (red) e) huDHFR/NADPH/1006 (orange, yellow) and SaDHFR/NADPH/1006 (cyan) f) huDHFR/NADPH/1006 (orange, yellow) and huDHFR/NADPH/SRI-9662 (blue)

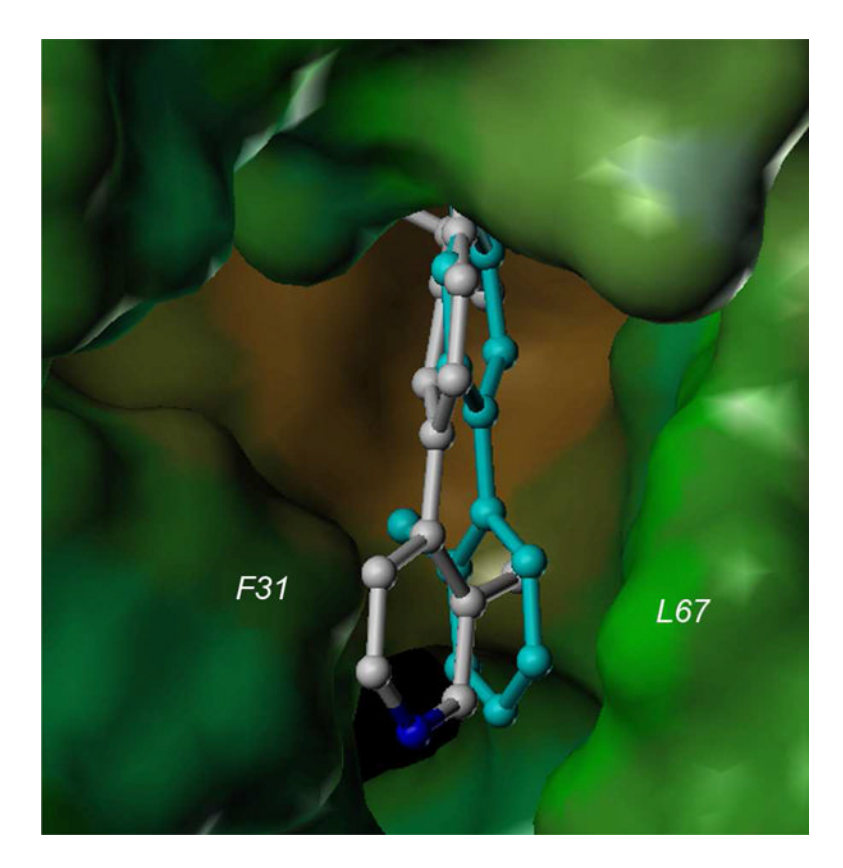


Figure 3. Docked complex of UCP1075 to human DHFR. Two representative poses (white and cyan) are shown, both of which show steric interference with Leu 67 and Phe 31. The active site is shown as a lipophilic surface.

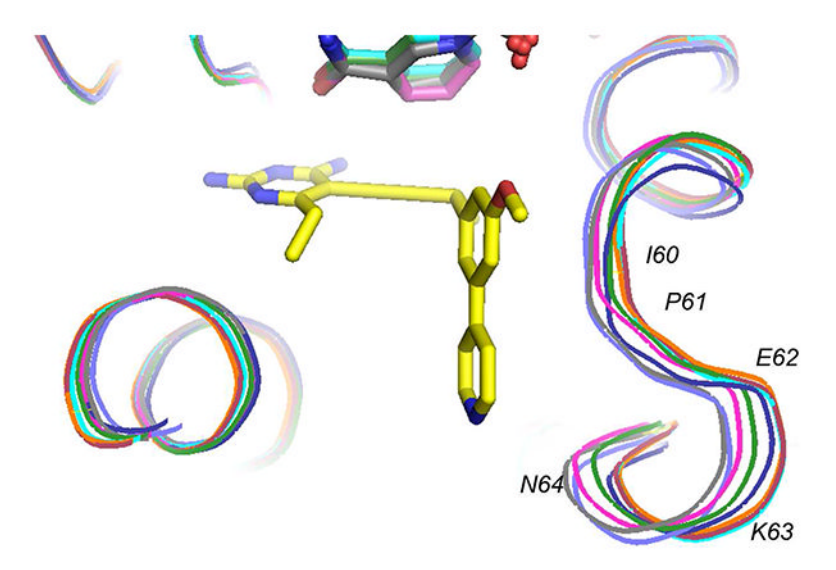


Figure 4. Superpositions of loop region (60-64) in a survey of crystal structures of human DHFR bound to a variety of ligands (4KAK: orange, 1KMV: periwinkle, 1S3W: green, 3NZD: magenta, 2C2S: light blue, 2W3A: raspberry, 1OHJ: dark blue, 4DDR: light gray).

Table 1
Propargyl-linked Antifolates Inhibit Human DHFR

Compound	IC ₅₀ Human DHFR (nM)
NH ₂ T 2 OMe	1300
UCP1006	
NH ₂ OMe	61
UCP1015	
NH ₂ OMe	60
UCP1017	
NH ₂ OMe	45
UCP1019	
NH ₂ N N N N N N N N N N N N N N N N N N N	330
UCP1025	
NH ₂ OMe	164
UCP1040	
OMe NH ₂ N	2641
UCP1075	
NH ₂ OMe	329
UCP1076	

Compound	IC ₅₀ Human DHFR (nM)
NH ₂ OMe	243
UCP1077	

Table 2

NIH-PA Author Manuscript

Data collection and refinement statistics

	hu/NADPH/UCP1006	hu/NADPH/UCP1025	hu/NADPH/UCP1017	hu/NADPH/UCP1019	hu/NADPH/UCP1015
PDB ID	4KAK	4KD7	4KFJ	4KEB	4KBN
Space Group	$C222_1$	$C222_1$	$C222_1$	$C222_1$	$C222_1$
No. monomers in asymmetric unit	2	2	2	2	2
Unit cell (a, b, c in Å)	88.08, 93.63, 96.04	87.67, 93.78, 95.99	87.81, 94.08, 96.29	87.71, 93.66, 96.16	105.26, 105.25, 144.68
Resolution (Å)	1.8	1.84	1.76	1.45	2.72
Completeness % (last shell, %)	(26.66) 87.66	99.53 (99.88)	(86.86) 89.86	99.37 (99.90)	(20.26) (67.67)
Unique reflections	37016 (3661)	34461 (3390)	39301 (3880)	69737 (6951)	21954 (2098)
Redundancy	3.95	4.2	8.1	8	8.1
R _{sym} , (last shell)	0.061 (0.492)	0.071 (0.317)	0.060 (0.154)	0.052 (0.589)	0.076 (0.385)
$\langle I/\sigma \rangle$ (last shell)	12.51 (2.50)	6.86 (2.53)	51.44 (20.28)	32.38 (5.03)	30.89 (8.17)
R-factor/R _{free}	0.2243/0.2666	0.2232/0.2716	0.1980/0.2451	0.1681/0.2054	0.1704/0.2184
No. of atoms (protein, ligands, solvent)	3694	3762	3697	3803	3385
Rms deviation bond lengths (Å), angles (deg)	0.006	0.013	0.014	0.016	0.013
Average B factor for protein (Å ²)	16.5	34.7	18.5	25.6	33.8
Average B factor for ligand $(Å^2)$	21.7	33.8	26.9	35.28	32.07
Average B factor for solvent molecules (\mathring{A}^2)	29.5	42.7	26.5	39.7	36.1
Residues in most favored regions (%)	91.8	91.8	90.3	93.1	94
Residues in additional allowed regions (%)	8.2	8.2	9.7	6.9	0.9
Residues in generously allowed regions (%)	0	0	0	0	0
Residues in disallowed regions (%)	0	0	0	0	0